Acta Metall. Sin. (Engl. Lett.), 2015, **28**(8), 1008–1014
DOI 10.1007/s40195-015-0288-7

Effect of Intergranular Precipitation on the Internal Oxidation Behavior of Cr–Mn–N Austenitic Stainless Steels

Lei-Gang Zheng[1] · **Xiao-Qiang Hu**[1] · **Xiu-Hong Kang**[1] · **Dian-Zhong Li**[1]

Received: 5 January 2015 / Revised: 6 March 2015 / Published online: 10 June 2015

Abstract The effect of intergranular precipitation on the internal oxidation behavior of Cr–Mn–N austenitic steels at 1000 °C in dry air atmosphere was investigated using scanning electron microscope, transmission electron microscope, and X-ray diffraction analysis. The results show that intergranular $M_{23}C_6$ carbide morphologies play an important role on the internal oxidation behavior of Cr–Mn–N steels. During the period of the oxidation, both discontinuous chain-shaped and continuous film-shaped intergranular $M_{23}C_6$ carbides precipitated along the grain boundaries. Internal oxides of silica preferentially intruded into the matrix along grain boundaries with discontinuous $M_{23}C_6$ carbide particles, while silica was obviously restricted at the interfaces between the external scale and matrix on the occasion of continuous film-shaped $M_{23}C_6$ carbides. It is seemed that reasonable microstructure could improve the oxidation resistance of Cr–Mn–N steels.

KEY WORDS: **$M_{23}C_6$ precipitation; Internal oxidation; Cr–Mn–N austenitic steel**

1 Introduction

Cr–Mn–N austenitic steels are considered as potential heat-resistant materials due to their good high-temperature mechanical properties at a relatively low cost [1, 2]. However, with the increase in Mn content in Cr–Mn–N steels, the oxidation resistance decreased significantly due to the formation of manganowustite and bulky Mn-rich nodules [3, 4]. To obtain maximum protection against oxidation, sufficient Cr content is needed to form a continuous and protective Cr_2O_3 scale when the alloys are applied in aggressive environments [5–7].

Moreover, the addition of Si or Al elements could effectively decrease the growth rate of the protective scale attributing to the formation of continuous inner silica- or alumina-healing layer [8–11]. Furthermore, the internal silica intrusions along the grain boundaries with cellular network morphology in silicon-containing austenitic stainless steels could improve the resistance of external oxide scale to spallation by mechanical keying effect [12, 13]. Therefore, understanding the internal oxidation process and its influencing factor is important for improving the oxidation resistance.

The process of internal oxidation is dominated by the diffusion of oxygen through the oxide scales and the alloy matrix and the diffusion of alloy elements toward the oxidation front [14, 15]. As a result, the internal oxidation preferentially takes place at the grain boundaries or other defects due to the fast diffusion at these positions [16, 17]. On the other hand, intermetallics such as Laves and Chi phases would precipitate along the grain boundaries or within the grains during the oxidation process, which may decrease the transport of metal cations and consequently affect the oxidation behavior [18–20]. Horita et al. [18, 19] revealed that the growth rate of external scale was obviously reduced due to the decrease in chromium diffusivity

---

Available online at http://link.springer.com/journal/40195

✉ Xiao-Qiang Hu
xqhu@imr.ac.cn

[1] Shenyang National Laboratory for Materials Science, Institute of Metal Research, Chinese Academy of Sciences, Shenyang 110016, China

along the grain boundaries caused by the intergranular Laves phase in a ferritic stainless steel. Moreover, the oxidation kinetics could be slowed down by the degradation of chromium diffusion in oxide scale resulted from the prevention of chromium vacancy annihilation by Chi phase formed at the scale–alloy interface, as reported by Yun et al. [20] in tungsten-containing Fe–22Cr–0.5Mn steels. However, in considering the influence of intergranular carbides on internal oxidation, there is no information available in the previous work.

In the present study, the microstructure evolution and oxidation behavior of several Cr–Mn–N austenitic steels at 1000 °C in dry air atmosphere were investigated using scanning electron microscope (SEM), transmission electron microscope (TEM), and X-ray diffraction (XRD) analysis. The effects of intergranular precipitation on the internal oxidation behavior of the studied steels were discussed.

Table 1 Chemical compositions of the studied steels (wt%)

Steel	C	Si	Mn	Cr	Ni	N	Fe
Cr–Ni	0.31	0.67	1.49	25.60	10.37	0.12	Bal.
Cr–Mn–N-1	0.24	1.96	9.49	20.71	1.88	0.36	Bal.
Cr–Mn–N-2	0.29	1.80	11.09	20.01	2.00	0.35	Bal.
Cr–Mn–N-3	0.32	2.12	10.10	19.97	2.10	0.31	Bal.

2 Experimental

Cr–Mn–N austenitic steels were melted in a vacuum induction furnace (ZG-0.025F) and cast under inert gas protection. The chemical compositions of the Cr–Mn–N steels and a conventional commercial Cr–Ni steel are given in Table 1. Specimens of the steels for oxidation tests with a dimension of 15 mm × 12 mm × 9 mm were cut by wire electrode cutting machine, and the solution annealed at 1150 °C for 2 h. After that, the surfaces of the specimens were grinded by emery papers with different grits (No. 150—No. 2000). Prior to the oxidation experiments, the grinded specimens were ultrasonically cleaned in ethanol

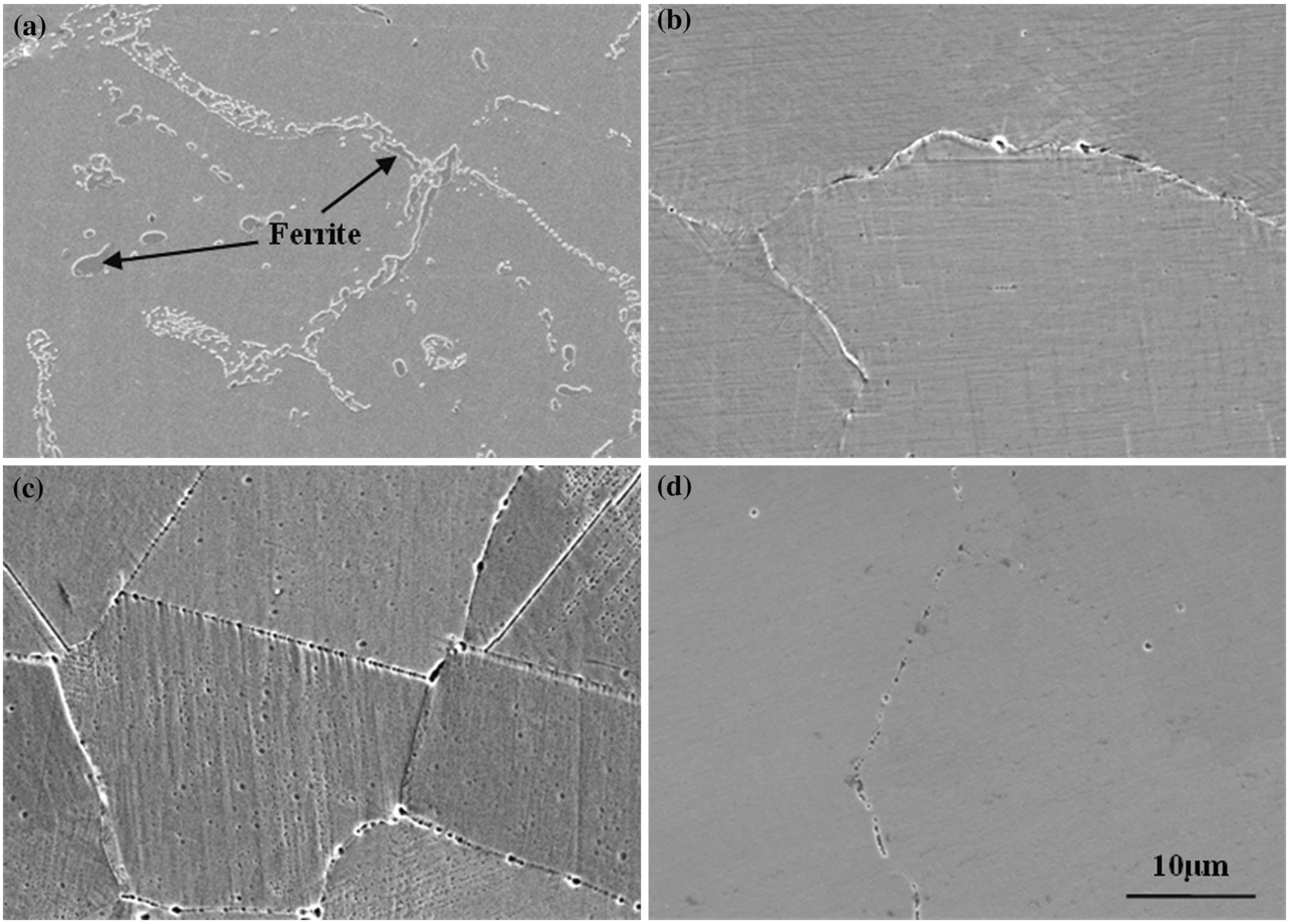

Fig. 1 SEM micrographs of the Cr–Ni **a**, Cr–Mn–N-1 **b**, Cr–Mn–N-2 **c**, Cr–Mn–N-3 **d** steels after solution-annealing treatment, respectively

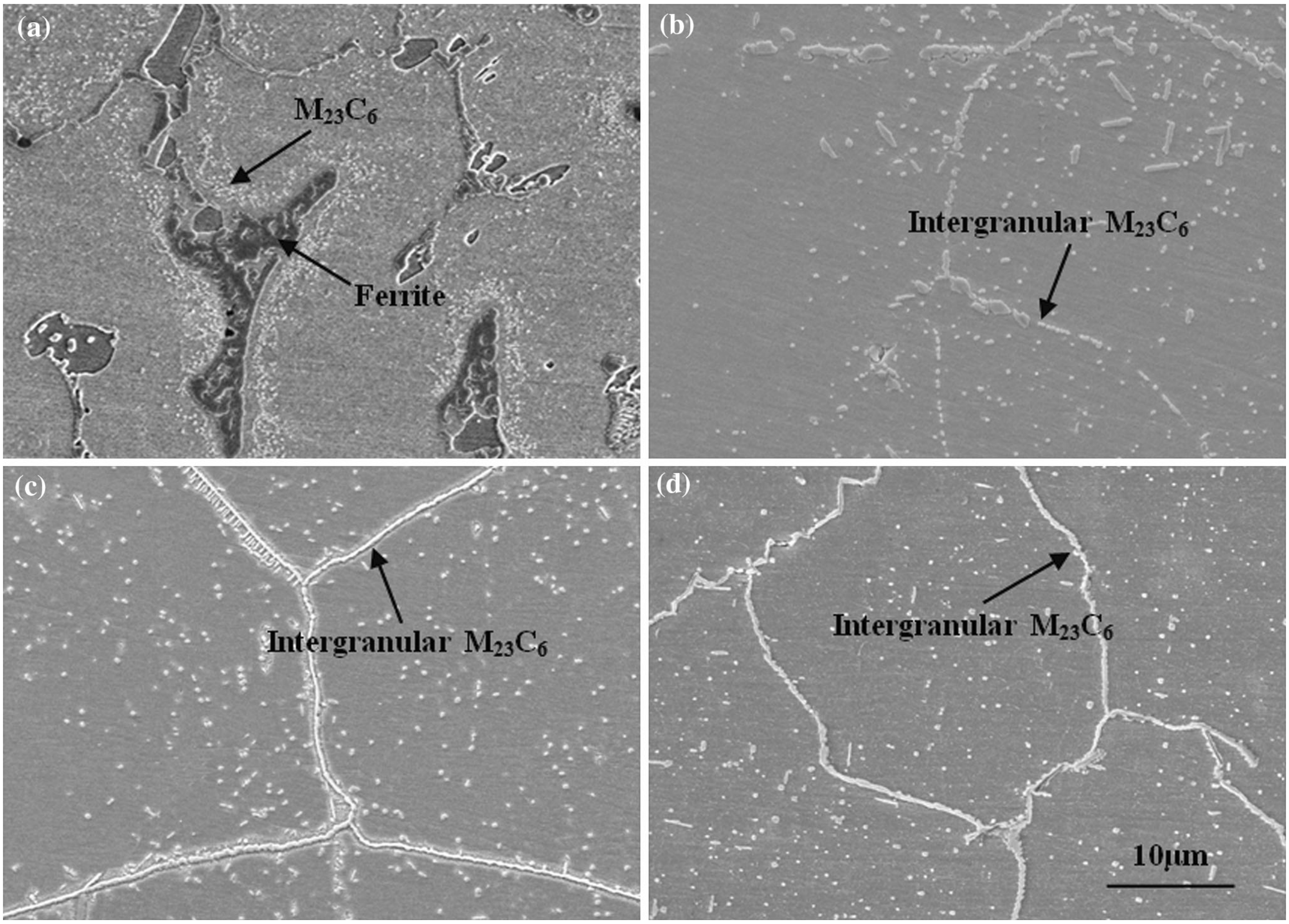

Fig. 2 SEM micrographs of the Cr–Ni **a**, Cr–Mn–N-1 **b**, Cr–Mn–N-2 **c**, Cr–Mn–N-3 **d** steels after oxidation at 1000 °C for 500 h in dry air atmosphere, respectively

for 15 min and dried by a blower. Subsequently, isothermal oxidation tests were carried out at 1000 °C in dry air atmosphere for 1, 5, 10, 70, 200, 300, and 500 h in Al_2O_3 chambers, respectively.

The oxidized specimens were examined in XRD (D/Max-2500 PC) to confirm the composition of the oxide scale. Then, the oxidized specimens were embedded in epoxide resin followed by grinding and polishing. Subsequently, the specimens were etched by aqueous aqua regia (15 mL HCl + 5 mL H_2SO_4 + 80 mL H_2O) and observed by SEM (Hitachi S-3400 N) equipped with energy-dispersive spectrometer (EDS, Oxford IE3500). Samples for TEM observation were prepared in a twin-jet electrolytic polishing apparatus (Struers Tenupol-5) using a solution containing 10% perchloric acid and 90% ethanol at the temperature of −20 °C and employing a voltage of 20 V. Then, those samples were examined using a Tecnai G2 F20 TEM operating at 200 kV.

3 Results and Discussion

3.1 Microstructure Evolution During the Period of Oxidation

Figure 1 shows the SEM maps of the microstructure of the studied steels after solution-annealing treatment at 1150 °C. As shown in Fig. 1a, the Cr–Ni steel had a duplex-phase microstructure with some isolated ferrite islands distributed on the austenite matrix and discontinuous ferrite chains along the grain boundaries. However, the Cr–Mn–N steels were observed with complete austenite microstructure without any precipitates on the grain boundaries, as indicated in Fig. 1b–d.

After oxidation at 1000 °C for 500 h, the microstructure of the studied steels is illustrated in Fig. 2. Some $M_{23}C_6$ particles were observed around the ferrite phase in the Cr–Ni steel (Fig. 2a). For the Cr–Mn–N steels, $M_{23}C_6$ carbides

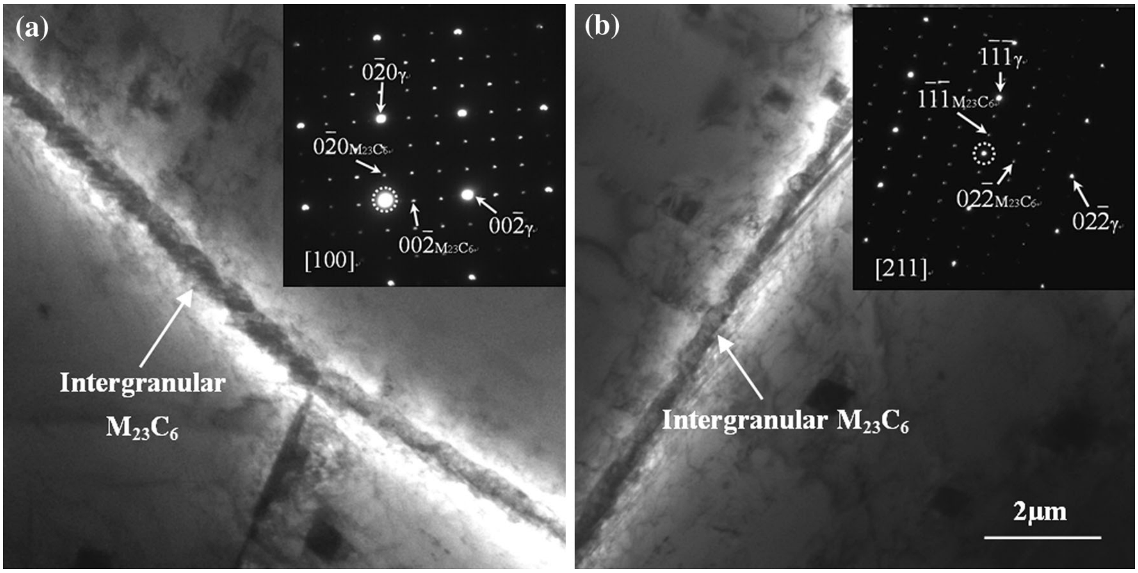

Fig. 3 TEM bright field images and corresponding SAED patterns of $M_{23}C_6$ on grain boundaries in Cr–Mn–N-2 **a** and Cr–Mn–N-3 **b** steels. (The corresponding SAED patterns in **a** and **b** showed a cube-on-cube orientation relationship of $[001]_\gamma//[001]_{M_{23}C_6}$, $\left((100)_\gamma//(100)_{M_{23}C_6}\right)$ and $[211]_\gamma//[211]_{M_{23}C_6}$, $\left((111)_\gamma//(111)_{M_{23}C_6}\right)$ between $M_{23}C_6$ carbides and the matrix, respectively)

precipitated both within the matrix and on the grain boundaries during long term oxidation at high temperature. The intergranular $M_{23}C_6$ carbides in Cr–Mn–N-2 and Cr–Mn–N-3 steels were observed in continuous film-shaped morphology (Fig. 2c, d), while the intergranular $M_{23}C_6$ carbides in Cr–Mn–N-1 steel were in discontinuous chain-shaped morphology along the grain boundaries (Fig. 2b). TEM images and corresponding selected-area electron diffraction (SAED) patterns of the intergranular $M_{23}C_6$ carbides in Cr–Mn–N-2 and Cr–Mn–N-3 steels are shown in Fig. 3. The results indicated that the intergranular $M_{23}C_6$ carbides kept a cube-on-cube orientation relationship with one of the two grains beside the grain boundary.

As suggested by Yamaura et al. [17], the grain boundaries are preferential areas where the internal oxidation takes place. The precipitates that formed along the grain boundaries during the oxidation process could block the fast diffusion path for the diffusion of oxygen into the matrix from the scale and the diffusion of alloy elements out from the matrix [19]. Therefore, the microstructure evolution is an important factor that affects the internal oxidation behavior of the studied steels in the long-term duration at high temperature.

3.2 Internal Oxidation Behavior

Figure 4 shows the cross-sectional SEM images of the oxide scales for the studied steels after isothermal oxidation at 1000 °C for 1 h in dry air atmosphere. A continuous external oxide scale with a few microns in thickness was present on the surfaces of all the samples. For the Cr–Mn–N steels, a discontinuous internal oxide layer of silica formed at the scale–alloy interfaces. In addition, some internal oxides started to intrude into the alloy matrix (Fig. 4b–d). In the case of Cr–Ni steel, however, no obvious internal oxides were observed beneath the external scale (Fig. 4a). This phenomenon is related to the difference of chemical compositions among these steels. The content of chromium in the Cr–Ni steel (25.6 wt%) is higher than that in the Cr–Mn–N steels (about 20 wt%), and the content of silicon in Cr–Ni steel (0.67 wt%) is much lower than that in Cr–Mn–N steels ((1.80–2.12) wt%). Correspondingly, the oxidation of chromium instead of silicon in the Cr–Ni steel has dominated the oxidation behavior at the initial oxidation stage.

The composition of the oxide scales for the studied steels oxidized at 1000 °C for 1 h analyzed by EDS is presented in Table 2. The results showed that the oxide scale was identified as chromium-rich oxides for the Cr–Ni steel, while the oxide scales formed on Cr–Mn–N steels were rich in manganese and chromium. Meanwhile, the XRD patterns of the oxide scales corresponded to mixed cubic oxide M_2O_3 ($(Mn, Cr)_2O_3$), as shown in Fig. 5. For the Cr–Ni steel, the M_2O_3 is close to Cr_2O_3, while the M_2O_3 in Cr–Mn–N steels is close to Mn_2O_3.

The cross-sectional SEM backscattered electron images of the samples after isothermal oxidation at 1000 °C for 500 h in dry air atmosphere are shown in Fig. 6. The thin outer layer of spinel oxides ($MnCr_2O_4$ for Cr–Ni steel and $MnFe_2O_4$ for Cr–Mn–N steels) peeled off from the surfaces

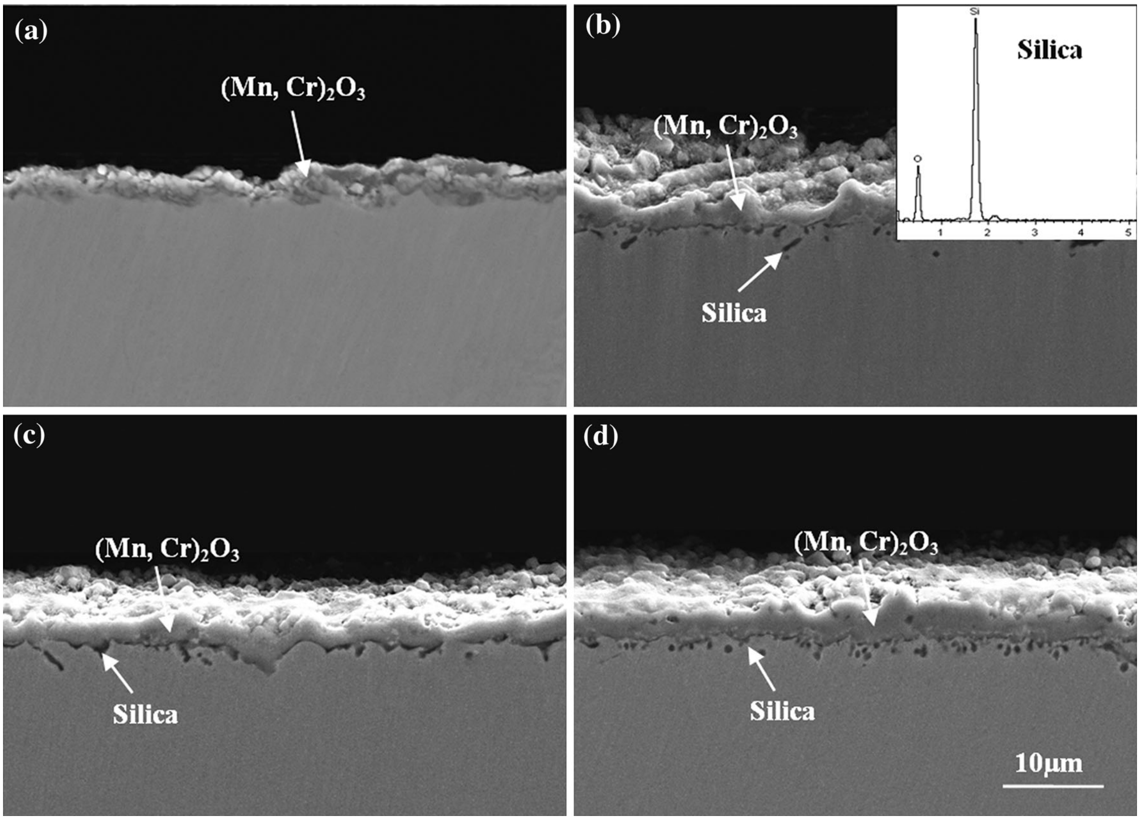

Fig. 4 Cross-sectional SEM secondary electron images of the Cr–Ni **a**, Cr–Mn–N-1 **b**, Cr–Mn–N-2 **c**, Cr–Mn–N-3 **d** steels isothermally oxidized at 1000 °C for 1 h in dry air atmosphere, respectively (The EDS spectrum in **b** showed that the internal oxides are silica)

Table 2 Composition of the oxide scales for the studied steels oxidized at 1000 °C for 1 h analyzed by EDS (wt%)

Steel	O	Mn	Cr	Fe
Cr–Ni	31.47	10.91	54.66	1.11
Cr–Mn–N-1	25.96	42.43	26.17	5.44
Cr–Mn–N-2	20.69	50.56	23.14	5.61
Cr–Mn–N-3	20.84	53.96	19.21	6.00

of the samples due to the thermal stress, leaving a thick scale of (Mn, Cr)$_2$O$_3$ on the top of the alloy matrix. Obviously, the internal oxidation behaviors showed different characteristics among the studied steels. In the case of Cr–Ni steel, a large amount of internal silica was observed beneath the external oxide scale. Moreover, the internal silica intruded deeply into the alloy matrix along the interfaces between ferrite and austenite, as indicated by the arrows in Fig. 6a. Similarly, the internal oxides preferentially grew into the alloy matrix along the grain boundaries in Cr–Mn–N-1 steel, as marked by the arrows in Fig. 6b. On the contrary, the internal oxidation behavior of Cr–Mn–N-2 and Cr–Mn–N-3 steels was rather different from that of Cr–Mn–N-1 steel. Only a few silica in a thin layer or isolated particles was observed at the (Mn, Cr)$_2$O$_3$ scale–alloy interface (Fig. 6c, d), which is similar to the results after oxidation for 1 h (Fig. 4c, d). It is difficult to be explained only by considering the composition difference among these steels. All the studied Cr–Mn–N steels have the extremely similar content of alloy elements,

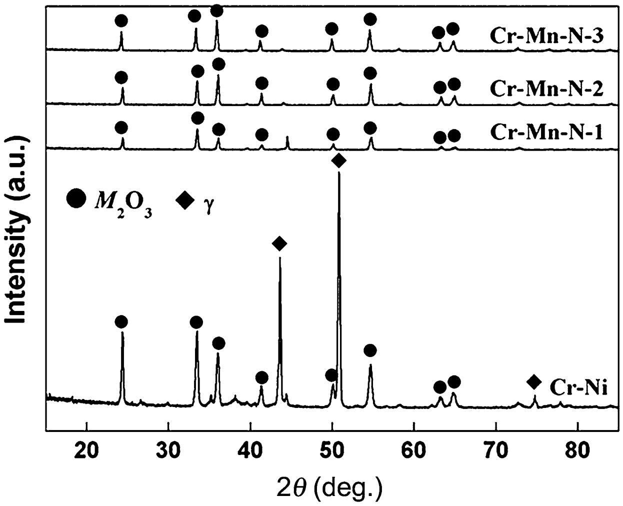

Fig. 5 XRD patterns for the oxide scales of the studied steels oxidized at 1000 °C for 1 h

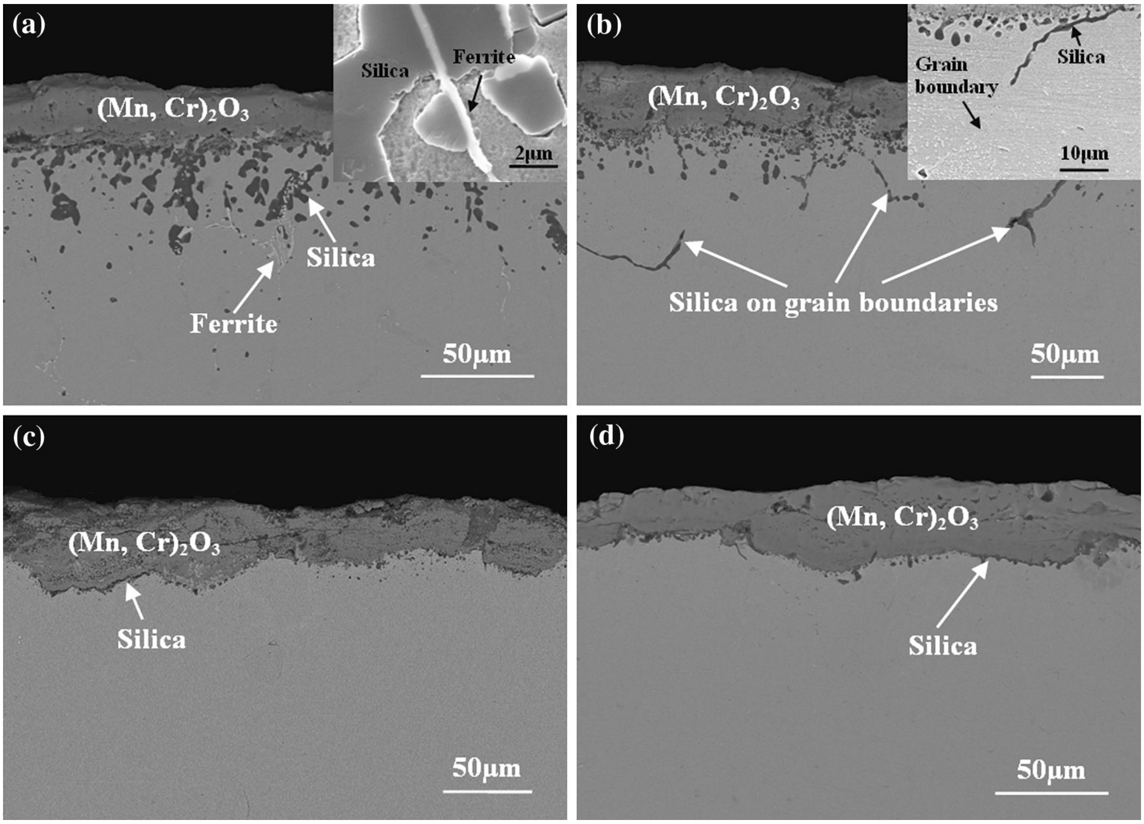

Fig. 6 Cross-sectional SEM backscattered electron images of Cr–Ni **a**, Cr–Mn–N-1 **b**, Cr–Mn–N-2 **c** Cr–Mn–N-3 **d** steels isothermally oxidized at 1000 °C for 500 h in dry air atmosphere, respectively (The *small images inserted* in **a** and **b** displayed the details that silica intruded along austenite–ferrite interfaces and grain boundaries, respectively)

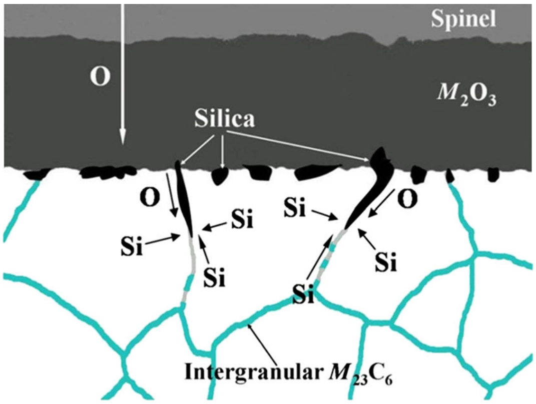

Fig. 7 Schematic map for the oxidation process of the studied Cr–Mn–N steels

especially for the oxidation-resistant elements of Cr and Si. Therefore, the internal oxidation behaviors are probably restrained by the blocking of oxygen and metal element diffusion attributing to the intergranular precipitation of $M_{23}C_6$ carbides.

3.3 Effect of Intergranular $M_{23}C_6$ on the Internal Oxidation Behavior

Figure 7 is a schematic map which demonstrates the oxidation process of the studied Cr–Mn–N steels. At the initial oxidation stage, a thin film of Cr_2O_3 immediately formed because of the greater negative Gibbs free energy for the oxidation reaction between chromium and oxygen [21]. With the continuous oxidation, the volatilization of Cr_2O_3 takes place at the temperature up to 1000 °C [22, 23]. Consequently, the initial oxide scale becomes porous. And it is incapable of inhibiting the outward diffusion of the metal cations such as Fe^{2+} and Mn^{2+} that results in the formation of MO oxides (FeO or MnO) on the surface. Subsequently, the MO oxides are continuously oxidized into M_2O_3 or combined with Cr_2O_3 to form the spinel oxides ($MnCr_2O_4$ or $MnFe_2O_4$). Eventually, the top surface is covered with a uniformly distributed spinel layer. This layer is effective to protect M_2O_3 from volatilizing and decrease the outward diffusion of metal cations and hinder the outer spinel layer thickening. Meanwhile, M_2O_3 layer could continuously grow toward the matrix because the outer spinel layer could not restrict the inward diffusion of oxygen [24].

The presence of internal silica at the scale–alloy interface is attributed to the reaction of silicon with oxygen which diffuses from the oxide scale. According to the Wagneŕs oxidation model [14], further growth of internal silica needs the transport of oxygen and silicon in the alloy matrix [25]. Oxygen continuously diffuses along the silica–alloy interfaces and reacts with silicon which is transported to the reaction front along the grain boundaries or from the interiors of adjacent grains by lattice diffusion. This diffusion process leads to the intergranular intrusion of silica, as illustrated in Fig. 7. The greater depth of the internal silica intrusion along the grain boundaries and the phase interfaces in the Cr–Mn–N-1 and Cr–Ni steels suggest that the flux of oxygen along these defects is much larger than that in the alloy matrix (Fig. 6a, b). Nevertheless, in the Cr–Mn–N-2 and Cr–Mn–N-3 steels, those preferential diffusion paths of the grain boundaries are almost wholly occupied by the intergranular film-shaped $M_{23}C_6$ carbides, which retard the formation of silica by blocking the oxygen and silicon diffusion [18–20]. Therefore, the growth rate of internal silica is considerably reduced, consequently leading to the morphologies of internal silica at the scale–alloy interface in Cr–Mn–N-2 and Cr–Mn–N-3 steels (Fig. 6c, d).

The effects of chemical compositions and oxidation environments on the oxidation mechanism of metals are particularly emphasized by the previous work, whereas the relationship between the microstructures and oxidation resistance of alloys is often unfortunately neglected. The facts [13, 18–20, 26] suggested that the growth of the oxide scale could be significantly reduced by fined grains and intermetallics in some alloys. In addition, the adherence of oxide scale to alloy matrix could be increased considerably by the presence of fine, uniform dispersion of intermetallic or nonmetallic precipitates [27]. In the present work, the growth of internal silica was effectively suppressed by the intergranular film-shaped $M_{23}C_6$ carbides. Therefore, the oxidation resistance of the alloys could be promoted by an alternative of the appropriate heating procedure to obtain reasonable microstructures. And it also inspires that the improvement in oxidation resistance at high temperature should be focused not only on the addition of some oxidation-resistant elements but also on the microstructure control. Further investigation about the influence of microstructures on the oxidation behavior of Cr–Mn–N austenitic stainless steels is still in progress, and more information will be shown in the future.

4 Conclusions

1. During the isothermal oxidation at 1000 °C in dry air atmosphere, both the discontinuous chain-shaped and continuous film-shaped intergranular $M_{23}C_6$ carbides precipitate in the studied Cr–Mn–N austenitic stainless steels. The film-shaped intergranular $M_{23}C_6$ carbides retain a cube-on-cube orientation relationship with one of the two grains beside the grain boundary.
2. Internal oxidation of silicon takes place beneath the external oxide scale during the oxidation process. The internal oxides grow preferentially along the grain boundaries or the phase interfaces where the film-shaped intergranular $M_{23}C_6$ is absent. The intrusion of internal oxides into alloy matrix is effectively suppressed by the continuous intergranular $M_{23}C_6$ carbides.

Acknowledgments This work was financially supported by the National Natural Science Foundation of China (No. 51301175).

References

[1] C.M. Hsiao, Acta Metall. Sin. **3**, 138 (1958). **(in Chinese)**
[2] Y.K. Li, Y.H. Hsieh, Y.Y. Kuo, C.H. Shih, Acta Metall. Sin. **9**, 33 (1966). **(in Chinese)**
[3] P.R.S. Jackson, G.R. Wallwork, Oxid. Met. **21**, 135 (1984)
[4] D.L. Douglass, F. Gesmundo, C. de Asmundis, Oxid. Met. **25**, 235 (1986)
[5] X.Q. Xu, X.F. Zhang, G.L. Chen, Z.P. Lu, Mater. Lett. **65**, 3285 (2011)
[6] A.M. Huntz, A. Reckmann, C. Haut, C. Sévérac, M. Herbst, F.C.T. Resende, A.C.S. Sabioni, Mater. Sci. Eng. A **447**, 266 (2007)
[7] X. Peng, J. Yan, Y. Zhou, F. Wang, Acta Mater. **53**, 5079 (2005)
[8] D. Caplan, M. Cohen, J. Electrochem. Soc. **112**, 471 (1965)
[9] F.H. Stott, G.C. Wood, Mater. Sci. Eng. A **87**, 267 (1987)
[10] E. Essuman, G.H. Meier, J. Żurek, M. Hänsel, L. Singheiser, W.J. Quadakkers, W.J. Quadakkers, Scr. Mater. **57**, 845 (2007)
[11] F.H. Stott, G.C. Wood, J. Stringer, Oxid. Met. **44**, 113 (1995)
[12] G.J. Yurek, D. Eisen, A. Garratt-Reed, Metall. Trans. A **13**, 473 (1982)
[13] H. Fujikawa, T. Morimoto, Y. Nishiyama, S.B. Newcomb, Oxid. Met. **59**, 23 (2003)
[14] C. Wagner, J. Electrochem. Soc. **99**, 369 (1952)
[15] Y. Li, J.E. Morral, Acta Mater. **50**, 3683 (2002)
[16] A. Ul-Hamid, Oxid. Met. **58**, 23 (2002)
[17] S. Yamaura, Y. Igarashi, S. Tsurekawa, T. Watanabe, Acta Mater. **47**, 1163 (1999)
[18] T. Horita, H. Kishimoto, K. Yamaji, Y.P. Xiong, N. Sakai, M.E. Brito, H. Yokokawa, Solid State Ionics **179**, 1320 (2008)
[19] T. Horita, H. Kishimoto, K. Yamaji, Y.P. Xiong, N. Sakai, M.E. Brito, H. Yokokawa, J. Power Sources **176**, 54 (2008)
[20] D.W. Yun, H.S. Seo, J.H. Jun, J.M. Lee, D.H. Kim, K.Y. Kim, Int. J. Hydrogen Energy **36**, 5595 (2011)
[21] G.C. Wood, F.H. Stott, Mater. Sci. Technol. **3**, 519 (1987)
[22] D. Caplan, M. Cohen, J. Electrochem. Soc. **108**, 438 (1961)
[23] P. Berthod, Oxid. Met. **64**, 235 (2005)
[24] N. Sakai, T. Horita, Y.P. Xiong, K. Yamaji, H. Kishimoto, M.E. Brito, H. Yokokawa, T. Maruyama, Solid State Ionics **176**, 681 (2005)
[25] R.K. Wild, Corros. Sci. **17**, 87 (1977)
[26] G. Chen, H. Lou, Scr. Mater. **41**, 883 (1999)
[27] I.M. Allam, H.C. Akuezue, D.P. Whittle, Oxid. Met. **14**, 517 (1980)